ADVANCED MATERIALS
www.advmat.de

Long-Range Proton Channels Constructed via Hierarchical Peptide Self-Assembly

Semion Censor, Jorge Vega Martin, Ohad Silberbush, Samala Murali Mohan Reddy, Ran Zalk, Lonia Friedlander, Daniel G. Trabada, Jesús Mendieta, Guillaume Le Saux, Jesús Ignacio Mendieta Moreno, Linda Angela Zotti, José Ortega Mateo, and Nurit Ashkenasy**

The quest to understand and mimic proton translocation mechanisms in natural channels has driven the development of peptide-based artificial channels facilitating efficient proton transport across nanometric membranes. It is demonstrated here that hierarchical peptide self-assembly can form micrometers-long proton nanochannels. The fourfold symmetrical peptide design leverages intermolecular aromatic interactions to align self-assembled cyclic peptide nanotubes, creating hydrophilic nanochannels between them. Titratable amino acid sidechains are positioned adjacent to each other within the channels, enabling the formation of hydrogen-bonded chains upon hydration, and facilitating efficient proton transport. Moreover, these chains are enriched with protons and water molecules by interacting with immobile counter ions introduced into the channels, increasing proton flow density and rate. This system maintains proton transfer rates closely resembling those in natural protein channels over micrometer distances. The functional behavior of these inherently recyclable and biocompatible systems opens the door for their exploitation in diverse applications in energy storage and conversion, biomedicine, and bioelectronics.

1. Introduction

The transport of protons is fundamental to diverse biological processes, such as aerobic respiration and photosynthesis.[1,2] In such processes, protons traverse nanometer-scale distances across cellular membranes through specialized channels in membrane proteins. In these channels, fast proton transfer rates are achieved through the structurally orchestrated confinement of water molecules and protein side chains, fostering the creation of hydrogen-bonded chains that facilitate proton translocation.[3–5] Considerable scientific effort has been directed over the years to mimicking these efficient proton channel machineries,[6–8] with emphasis on design considerations such as nanometric dimensions, compatibility with lipid bilayer membranes, and the precise spatial arrangement of functional groups along the channel. In the design of biomimetic proton channels, peptide molecules have emerged as attractive building blocks, offering a synthetic modular tool – in the form of small molecules – for incorporating important protein features.[7–11] Such peptide nanochannels, in turn, serve as valuable tools for deciphering the mechanisms underlying proton transport in natural channels, thereby shedding light on processes such as selectivity and gating. The high proton transfer efficiency in both natural nanochannels and their synthetic counterparts makes their incorporation into advanced technologies attractive, for example,

S. Censor, O. Silberbush, S. M. M. Reddy, G. Le Saux, N. Ashkenasy
Department of Materials Engineering
Ben-Gurion University of the Negev
Beer-Sheva 84105, Israel
E-mail: nurita@bgu.ac.il

The ORCID identification number(s) for the author(s) of this article can be found under https://doi.org/10.1002/adma.202409248

DOI: 10.1002/adma.202409248

J. V. Martin, D. G. Trabada, J. I. M. Moreno, L. A. Zotti, J. O. Mateo
Departamento de Física Teórica de la Materia Condensada and Condensed Matter Physics Center (IFIMAC)
Facultad de Ciencias
Universidad Autónoma de Madrid
Madrid E-28049, Spain
E-mail: jose.ortega@uam.es

R. Zalk, L. Friedlander, N. Ashkenasy
Ilse Katz Institute for Nanoscale Science & Technology
Ben-Gurion University of the Negev
Beer-Sheva 84105, Israel

J. Mendieta
Departamento de Biotecnología
Universidad Francisco de Vitoria
Pozuelo de Alarcón, Madrid E-28223, Spain

in fuel cells and other energy applications.[12–14] However, the assimilation of such biomimetic proton nanochannels into applications of this nature necessitates scaling up the length of the nanochannels to the mesoscopic, and even microscopic, ranges, while preserving the nanometric channel cross section and maintaining low tortuosity – all of which are necessary to achieve efficient, long-range, proton transport.

Previous studies demonstrated that in similarity to various biopolymers[15–18] peptide systems allow proton transport over large distances.[19–25] In particular, a significantly high proton conductivity was measured for assemblies of D,L α-cyclic peptides.[26–28] These cyclic peptides (see Figure S1a, Supporting Information) self-assemble into an antiparallel β-sheet configuration due to backbone hydrogen bonding interactions, forming nanotubes with the side chains of the peptide pointing outward.[29–31] It has been shown that the lumen of such synthetic nanotubes do indeed function as selective membranal ion channels.[32–36] However, the reliance of proton transport in the nanotube films on peptide side chains indicated that this process occurs on the outer surface of the nanotubes and not in their lumen. We hypothesized that the high proton conductivity presented for these assemblies, which was shown to almost exceed the conductivity of Nafion - a benchmark proton conducting material,[28] is associated with the propensity of the cyclic peptide nanotubes to self-associate. We now reveal the formation of permeable nanochannels between the peptide nanotubes upon self-association, allowing for high efficiency proton transport. Using a variety of experimental tools and theoretical modeling, we show that the specific design of the cyclic peptide monomeric unit promotes the hierarchical assembly process and equips the formed nanochannels with titratable amino acid side chains. Previous studies demonstrated efficient water self-diffusion over large distances within peptide nanochannels.[9,37–39] Herein we extend the state of the art and reveal– to the best of our knowledge for the first time – the activity of the interstitial nanochannels as proton channels. We demonstrate the critical role of immobile counterions incorporated in these extended biomimetic nanochannels both as the source of protons, which thus determines their density, and as hydration mediators that affect the rate of proton transfer in the proton channels. Remarkably, we show that these systems promote water-assisted proton transport, akin to proton transport in protein channels but spanning unprecedented longer distances.

2. Hierarchical Assembly of D,L α-Cyclic Peptides

The self-assembly of D,L α-cyclic peptides into nanotubes frequently produces whisker-like structures with diameters ranging from tens to hundreds of nanometers,[26–29,31] suggesting a sequential assembly process in which peptide nanotubes align in a specific pattern. Our investigation focused on the amphiphilic cyclic peptide, $c(\underline{KF})_4$ (Figure S1a, Supporting Information), which is made up of four dyads of L-lysine and D-phenylalanine. Since the side chains of the peptide point out of the backbone ring, they can be used to tune the hierarchical assembly of the nanotubes and functionalize the structure. We hypothesized that this specific molecular configuration would not only support the formation of nanotubes with fourfold symmetry but also dictate their hierarchical organization. The peptide self-assembly was achieved in a 10: 90 water: acetonitrile mixture (1 mM). This approach eliminated the need for a buffer, thereby avoiding the presence of salts, which could have affected both the water response and charge conduction in the samples. The samples were equilibrated in sealed Eppendorf tubes at room temperature for two weeks before use. It is noteworthy that the samples remained stable in the assembly solution for extended periods and could be utilized even after a year without noticeable changes.

Atomic force microscopy (AFM) images confirmed the formation of micrometer-long whisker-like fibers (Figure S2a, Supporting Information). In most cases, the fibers' cross section diameter was tens of nanometers. Nevertheless, thinner fibers with a diameter of ≈4 nm were also observed (Figure S2b, Supporting Information) and the diameter was shown to increase in increments of roughly 2 nm attesting to the hierarchical assembly of the nanotubes into larger structures. Since the size of the assemblies preclude the use of single crystal X-ray methodologies to determine the structure at high resolution, we employed high-resolution cryogenic electron microscopy (cryo-EM) to further investigate the structure of the peptide assembly.[40–44] This method has emerged as a powerful technique for high-resolution determination of complex biological assemblies,[45] and has been applied in recent years to the determination of peptide assemblies with remarkable precision.[46–48] In a typical experiment, transmission electron microscopy (TEM) is utilized to capture 2D projection images of the studied structure at high resolution. Multiple projections are then used to reconstruct a 3D density map through iterative processes of particle alignment and averaging. 2D class averages of self-assembled samples of $c(\underline{KF})_4$ indicated structures with a periodicity of 4.7 ± 0.4 Å (**Figure 1a**), indicative of the peptide backbone β-sheet folding interactions. This typical β-sheet distance was clearly apparent in the fast Fourier transform (FFT) analysis of the cryo-EM micrographs (Figure S3, Supporting Information). The self-assembly of $c(\underline{KF})_4$ into an anti-parallel β-sheet configuration was also confirmed by polarization modulation infrared reflection absorption spectroscopy (PM-IRRAS) (Figure S4, Supporting Information), and by the related diffraction plane peak in a grazing incidence X-ray diffraction (GIXD) spectrum (Figure S5, Supporting Information).

The 2D class averages of the cryo-EM micrographs revealed projections of single nanotubes (Figure 1a, left), as well as populations of hierarchically assembled nanotubes (Figure 1a; Figure S6, Supporting Information), in agreement with the AFM images. Single nanotube projections were used to reconstruct the 3D structure of the self-assembled nanotube (Figure 1b; Supplementary Video). To the best of our knowledge, this is the first example of direct imaging of cyclic peptide nanotubes. While the heterogeneity of the samples limited the resolution of the images, the lumen of the nanotube was clearly observed in the 3D map. 3D cryo-EM maps were also reconstructed from 2D class averages showing "double-filament" projections (Figure 1a, right). The density map revealed particles consisting of four nanotubes arranged in a rhombohedrum with a 1.9 nm edge length (Figure 1c; Supplementary Video). Indeed, this structural parameter was observed in powder X-ray Diffractions (XRD) diffractograms of $c(\underline{KF})_4$ samples (Figure S7 and Table S1, Supporting Information), and also in the FFT of the cryo-EM micrographs (Figure S3,

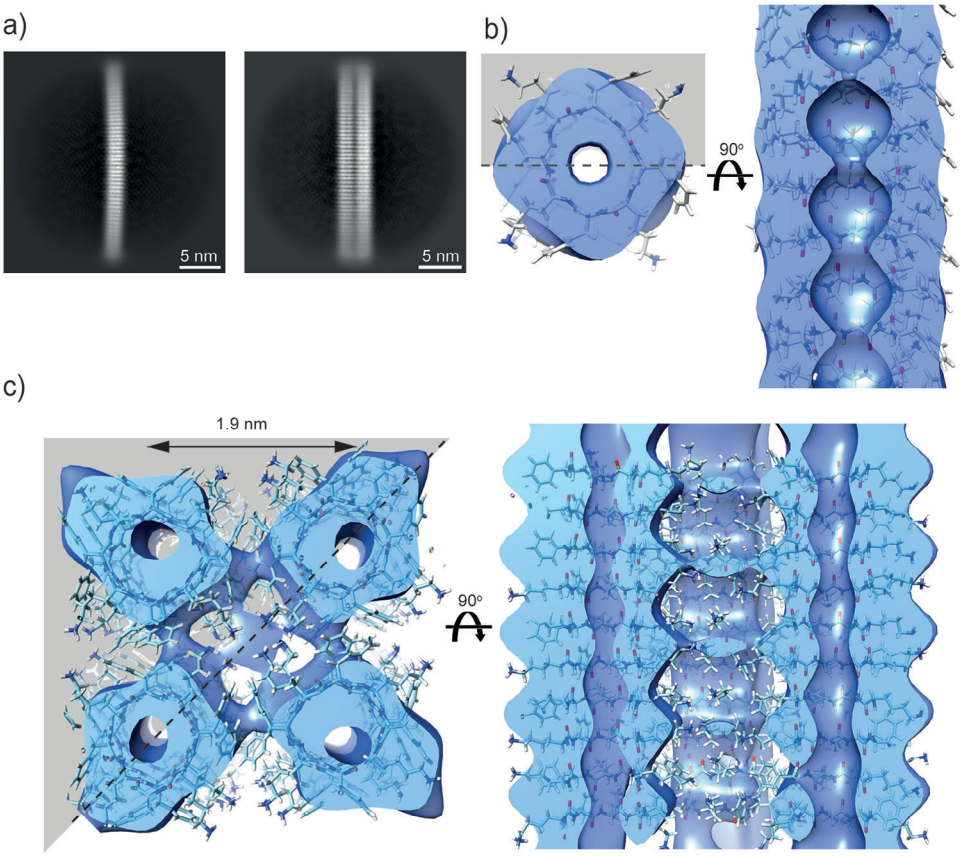

Figure 1. Hierarchical assembly of $c(\underline{KF})_4$. a) 2D class averages of a single particle and of two particles extracted from cryo-EM micrographs of $c(\underline{KF})_4$ assemblies. b) Surface representation of a 3D cryo-EM reconstruction of a single $c(\underline{KF})_4$ nanotube structure at a resolution of 5.9 Å. Slabs of the radial (left) and side (right) views are presented. The side view was clipped across the lumen of the nanotube. The section presented in the side view is highlighted in gray in the radial view. A rigid-body model extracted from the Molecular Dynamics (MD) simulations was fitted to the cryo-EM map using UCSF-CHIMERA.[49] A movie showing the 3D structure from different angles is provided in the Supplementary Information. c) Surface representation of a 3D cryo-EM reconstruction of four hierarchically assembled $c(\underline{KF})_4$ nanotubes at a resolution of 6.3 Å. Slabs of the radial (left) and side (right) views are presented. The side view was clipped across the diagonal of the rhombohedron structure formed by the hierarchical assembly of nanotubes. The section presented in the side view is highlighted in gray in the radial view. A rigid-body MD model was fitted to the cryo-EM map. A movie showing the 3D structure from different angles is provided in the Supplementary Information.

Supporting Information). Importantly, the reconstructed structure revealed that the hierarchical self-association of the nanotubes results in the formation of channels, with a diameter of ≈1.7 nm, between four contiguous nanotubes. Electron density was observed within this channel. This density can be explained by the presence of immobile atoms along the channel.

Molecular dynamics (MD) simulations were used to further investigate the self-assembly of $c(\underline{KF})_4$.[50] Initial studies on single nanotube assemblies revealed that a stack of six cyclic peptides is sufficient to ensure the formation of a self-assembled nanotube structure that is stable both in water and under vacuum. The tendency of the nanotubes to self-associate was confirmed by simulations obtained for four nanotubes consisting of a stack of 10 peptide molecules each (Figure 1c). In these simulations four nanotubes were arranged parallel to each other at the corners of a square with a side length of 22 Å, filled with water molecules and the system was allowed to relax (See supporting information for the procedure details). The resulting structure was in line with the cryo-EM reconstruction. The simulations showed that intermolecular hydrophobic aromatic interactions of the phenylalanine side chains induce the self-association of the nanotubes (**Figure 2a**). These interactions explain the appearance of a broad diffraction peak with a spacing of 3.9 Å, typical of aromatic interactions, in the XRD diffractograms (Figure S7 and Table S1, Supporting Information). Additional diffraction peaks with a *d*-spacing of 14–16 Å were assigned, according to the simulations, to the distances between planes rich in phenyl groups.

The inter-nanotube channels were clearly observed in the simulations. The simulations indicated that these interstitial channels are densely occupied by lysine side chains and are sheathed in a hydrophobic shell composed of the phenylalanine side chains (Figure 2a). Furthermore, the stability of the nanotube hierarchical assembly was maintained in the simulations for structures with 25% and 50% protonated amine side chains (Figure 2a; Figure S8, Supporting Information). Excess protonation of the amine side chains to levels of 75% and 100% was shown to destabilize the assembly, and the nanotubes drifted apart in the course of the simulations (100 ns). The trifluoroacetate counter ions (TFA^-) accounted for in the simulations to achieve charge balance, were found to occupy the interstitial channels (Figure 2a;

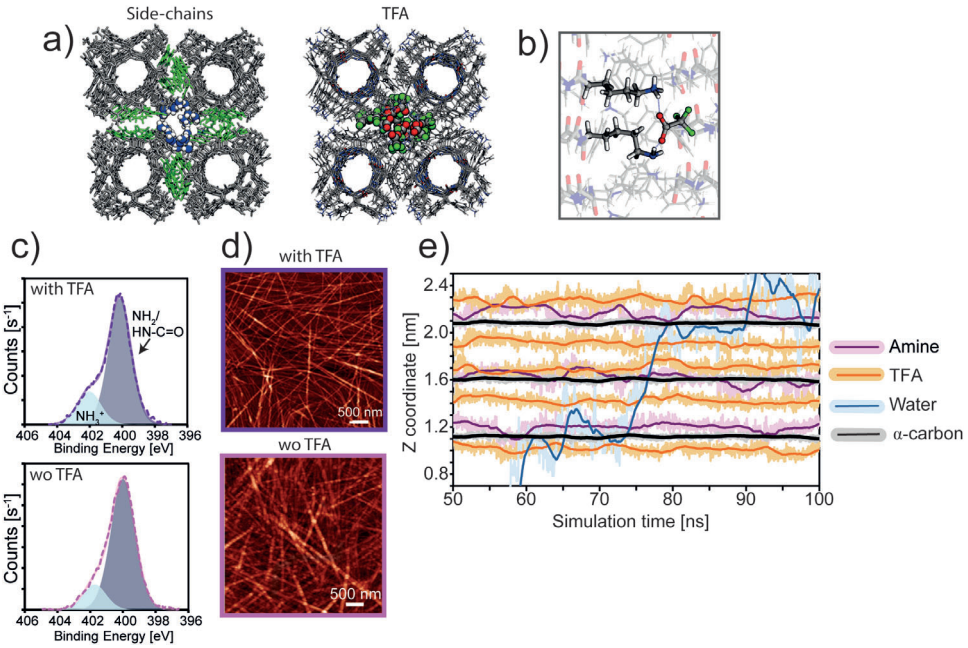

Figure 2. Characterization of counterion in the c(KF)$_4$ assembly. a) Top view snapshots of MD simulations highlighting side chain positions (amine in blue and white and phenyl in green) (left) and trifluoroacetate (TFA) ions (right) for an assembly of c(KF)$_4$nanotubes. Atoms within the inter-nanotube channel are indicated according to the following atomic color code: N – blue, H – white, O – red, C – gray, and F – green. The MD system consisted of a cluster of four nanotubes, each comprised of 10 c(KF)$_4$ peptide molecules; 50% of the lysine side chains were protonated and the system was fully hydrated. Side views of the snapshots of the MD simulation are presented in Figure S8 (Supporting Information). b) Snapshot of MD simulation showing a TFA ion bridging a protonated lysine and a non-protonated lysine of two adjacent peptide molecules. c) High-resolution X-ray Photoelectron Spectroscopy (XPS) N1s peak spectra of c(KF)4 assemblies in the presence of TFA and after TFA removal. The spectra were deconvoluted by using Advantage software. Residual protonated amines observed after the deprotonation process probably originated from ammonium hydroxide groups retained on the structure after drying. d) AFM topography images of c(KF)4 assemblies in the presence of TFA and after removal of TFA. The z scale is 60 and 80 nm for the images with and without TFA, respectively. e) Representative motion of TFA, lysine side chain, and water in the interstitial channel. Data was extracted over the last 50 ns of a 100-ns MD simulation for the periodic assembly model (see Experimental Section) with protonation of 50% of the lysine side chains and full hydration conditions. The z-axis corresponds to a range to ≈1.6 nm along the stack of nanotubes (roughly the length of a stack of three peptides). Black/gray lines represent the average position of the α-carbon atoms of three adjacent peptide molecule backbones along the simulation. Orange lines represent the motion of the center of mass of five TFA counterions. Purple lines represent the motion of the N atoms of three nearby lysine groups (the top and bottom amines are protonated, and the middle amine is unprotonated). Blue line represents one water molecule (O atom). The paler lines show the positions of frames obtained every 20 ps, while the darker solid lines show a moving average. Note, to improve clarity, nine lysine side chains, one TFA molecule, and about eleven water molecules are not presented.

Figure S8, Supporting Information), forming salt bridges with protonated lysine side chains and hydrogen bonds with neutral lysine groups (Figure 2b). These results suggest that the pKa of lysine in the assembled structure is much lower than in aqueous solution, as observed for lysine residues buried inside proteins.[51] X-ray photoelectron spectroscopy (XPS) experiments, conducted to confirm the presence of counterions in the system, indicated the presence of 7% fluorine atoms in the *c*(KF)$_4$ assembly (Table S2, Supporting Information), originating from the TFA used in the peptide purification process. High-resolution spectra of the N1S peak indicated that roughly 50% of the amines of the lysine side chains were protonated upon self-assembly of the peptides (Figure 2c), in agreement with the simulations. Treating the assemblies with an excess amount of base (NH_4OH) both in solution and after film deposition resulted in the deprotonation of the amine groups and an order of magnitude reduction in the concentration of fluorine in the samples (Figure 2c; Table S2, Supporting Information). AFM images (Figure 2d) and powder XRD data (Figure S7 and Table S1, Supporting Information) indicated that the structure remained intact in the deprotonated state, demonstrating that the presence of counterions is not essential for the integrity of the assemblies. Both the lysine side chains and the counterions were found to be relatively stationary (Figure 2e), with a very small calculated 1D diffusion coefficient of $\approx 2 \times 10^{-9}$ cm^2 s^{-1} for the TFA ions. The presence of stationary matter within the channels was confirmed in the experiments by the observation of atomic density in the channel in the reconstructed structure (Figure 1c). In contrast, the lumen of the nanotubes was found to be hollow, both in the experiments and in the simulation.

For purposes of comparison, we also studied the cyclic peptide, *c*(KY)$_4$, in which the phenyl groups of D-phenylalanine had been replaced by the phenol groups of D-tyrosine (Figure S1b, Supporting Information). A similar hierarchical assembly was observed for *c*(KY)$_4$, (Figure S9, Supporting Information). XPS experiments revealed a similar lysine protonation level due to the presence of counter ions (Figure S10 and Table S2, Supporting Information). It should be noted that the FTIR spectra indicates that the Tyr side chain is protonated (Figure S3, Supporting Information). This means that while the pKa of lysine and tyrosine

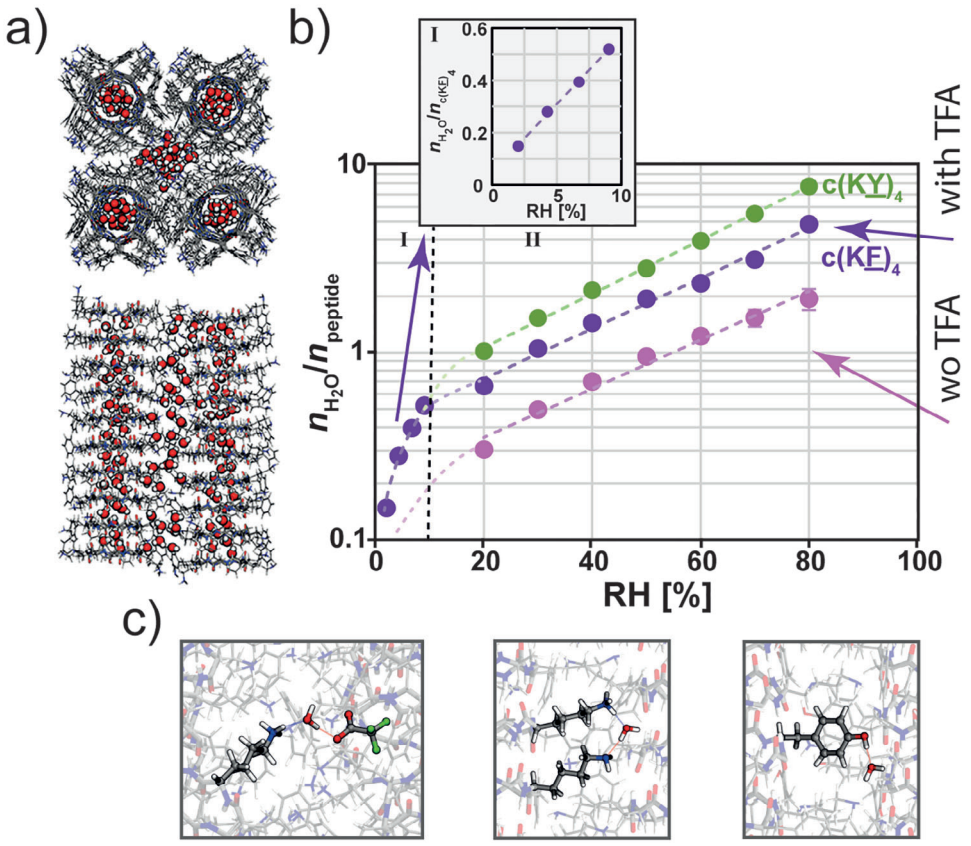

Figure 3. Hydration of the peptide assemblies. a) Top and side view snapshots of a MD simulation of a hydrated four-nanotube assembly with water molecules. The oxygen atoms of the water molecules are indicated in red. The positions of the amine groups (50% of which are protonated) and TFA ions are presented in Figure 2. b) Hydration isotherms of c(KF)$_4$ and c(KY)$_4$. Measurements were obtained on drop-cast films (ρ_0 = 16.5 μg•cm^{-2}), using a quartz crystal microbalance (QCM), after equilibration in a nitrogen atmosphere. The measurements were duplicated five and three times for c(KF)$_4$ and for c(KY)$_4$), respectively, except in the range of 0–10% RH, for which only one measurement was made. Averaged data is presented with the error calculated as the standard deviation. An example of the QCM raw data is provided in Figure S11 (Supporting Information). The two ranges of hydration are indicated with I and II on the main figure of (b). Absorption in range I is shown in the inset on a linear scale. Hydration of the c(KF)$_4$ film after TFA removal, indicating reduced hydration, is also shown. c) Snapshots of MD simulations showing: (left) a water molecule bridging a TFA ion and a protonated lysine side chain; (middle) a water molecule bridging protonated and non-protonated lysine side chains of two adjacent peptide molecules; and (right) a water molecule hydrogen bonded to a tyrosine side chain.

is similar in aqueous solution, it is different upon assembly because of differences in their local environment. While the *c*(KF)$_4$ assemblies presented a high persistent length, the *c*(KY)$_4$ assemblies were found to be more flexible (Figure S2a, Supporting Information). Nevertheless, powder XRD showed the two analogs to have a similar long-range order (Figure S7, Supporting Information), indicating the formation of stable hierarchically assembled nanotubes containing nanometric channels with an array of protonated amino acid side chains, which can lead to the formation of long-range hydrogen-bonded chains.

3. Hydration within the Peptide Nanochannels

Both the nanotube lumen and the interstitial channel are hydrophilic and can function as water channels, as demonstrated for various peptide assemblies.[9,37–39] Since formation of water channels may support efficient proton transport we set to investigate the hydration of the peptide assemblies. The presence of water in the nanotubes' lumen and in the interstitial channel was clearly observed in the MD simulations conducted in a water box (**Figure 3a**). The sorption of water was monitored experimentally by Quartz-Crystal Microbalance (QCM) as a function of relative humidity (RH) (Figure 3b; Figure S11, Supporting Information). An abrupt increase in water sorption was observed for the *c*(KF)$_4$ assembly in the lower humidity range of less than 10% RH (hydration range I), followed by an exponential increase in water sorption in the range 20–80% RH (hydration range II), resulting in an overall loading of about five water molecules per peptide molecule as the RH increased from 10% to 80%. The two-step sorption process can be explained by considering the different types of hydrogen bond formed in the system during hydration. The simulations showed that in the initial steps of sorption, water molecules are sorbed by hydrogen bonding to TFA ions and amine side chains incorporated into the inter-nanotube channels (Figure 3c; Figure S12, Supporting Information). This process, which probably governs water sorption in range I, is accompanied by a reduction in the number of lysine-TFA hydrogen bonds. As the number of water molecules in the

structure increases further, the hydrogen bonding interactions become saturated, and water molecules start to form hydrogen bonds between themselves, a process that is observed in range II. This mechanism was confirmed by hydration experiments of TFA free samples (Figure 3b), which showed that the sorption pattern does not change in range II, while in range I sorption seems to be largely suppressed. As a result, an overall lower hydration was observed in the absence of counterions. Indeed, the simulations indicated that the number of water molecules occupying the interstitial channel (which is 4.4 ± 0.9 and 4.0 ± 0.4 water molecules per peptide in the $c(\underline{KF})_4$ and $c(\underline{KY})_4$ assemblies for fully hydrated system with 50% protonated lysine side chains, respectively) drops by ~50% in the absence of counter ions, i.e., when the lysine side chains are not protonated. In contrast, the water density in the nanotubes' lumen remained unchanged, i.e., 4.25 ± 0.5 water molecules per peptide, for both $c(\underline{KF})_4$ and $c(\underline{KY})_4$ assemblies, regardless of the protonation state of the system, as expected. The MD simulations indicated efficient water self-diffusion in the lumen of the nanotubes (Table S3, Supporting Information), similar to other peptide-based water channels.[37,38] The water molecules were found to be tightly bound in the interstitial channel, probably due to the formation of stable hydrogen bonds with TFA and with lysine side chains,[39] leading to one to two orders of magnitude lower calculated diffusion coefficient for water molecules in the interstitial channel than in the lumen (Table S3, Supporting Information). It should be noted that water molecules are also adsorbed on the assembly surfaces. Similarly to the case of the interstitial channel, it should be expected that water molecules on the assembly surfaces would first be adsorbed to hydrogen bonding sites and then to other water molecules, with the second process being unlimited and thus yielding the formation of multilayers. Finally, when comparing $c(\underline{KF})_4$ and $c(\underline{KY})_4$ assemblies, greater water sorption was observed in the $c(\underline{KY})_4$ assembly (Figure 3b). This higher water uptake can be explained by hydrogen bonding to the hydroxyl groups of tyrosine's phenol side chains that replace the phenyl groups in $c(\underline{KF})_4$ (Figure 3c), especially on the outer surface of the nanotube bundles.

4. Proton Transport through Peptide Nanochannels

The formation of hydrogen bonding networks incorporating both water molecules and peptide side chains confined within a 1D space in the hierarchically assembled nanochannels provides the conditions for efficient proton transfer analogous to protein proton channels.[1] By virtue of the extended length of these biomimetic hierarchically assembled artificial channels, this proton transfer process can proceed over long distances. We used impedance spectroscopy (IS) to characterize the charge transport on films of the assemblies drop cast on interdigitated electrode (IDE) chips in parallel to the hydration experiments (**Figure 4a**; Figure S13, Supporting Information). The appearance of a semicircle in the Nyquist plots of the measurements attests to charge translocation through the film, over the gap between the electrodes, which was 5–25 µm. The inclined tail at the right of the semicircle is related to charge accumulation and polarization at the contacts' interface at lower frequencies. The resistance of the film, calculated from the diameter of the semicircle, decreased exponentially with increasing RH in hydration range II for both $c(\underline{KF})_4$ and $c(\underline{KY})_4$ assemblies (Figure S13, Supporting Information), as expected for proton charge carriers. For similar RH conditions, the resistance of the $c(\underline{KF})_4$ films was found to be about an order of magnitude lower than that of $c(\underline{KY})_4$, despite the higher water uptake of the latter assembly; this finding indicates that the conductivity of the assemblies is not solely related to their water uptake. Moreover, while an abrupt increase in the conductivity, of about six orders of magnitude, was observed for $c(\underline{KF})_4$ assemblies as hydration increased from 0.6 to 3 water molecules per peptide (Figure 4b), further water uptake resulted only in a slight increase in the conductivity, even though showing the same exponential dependence on relative humidity (Figure 4b). The above-described findings revealed a discernible heterogeneity in the modulation of proton transfer by water molecules within the studied system. It appears that initially absorbed water molecules that are situated in proximity to peptide side chains exert a pronounced influence on proton transfer dynamics. This notion, in turn, suggests that water molecules occupying interstitial channels and semi-open channels on the assemblies' surface dominate the proton transport processes, while subsequently formed water multilayers do not significantly impact the process, despite their substantial contribution to the volume of water in the film. The smaller involvement of bulk water to proton transport can explain the limited contribution of the nanotube lumens to proton conductivity, despite the higher water self-diffusion coefficient. However, we note that the absence of charge carriers in the lumen, which will be shown below, could be a dominant factor for the lower proton conductivity in the lumen as well.

The heterogeneous contribution of water molecules to the conductivity of the $c(\underline{KF})_4$ and $c(\underline{KY})_4$ assemblies also explains the different conductivity behaviors of the two types of assembly as a function of hydration, with $c(\underline{KF})_4$ assemblies exhibiting a steeper increase in conductivity and a faster saturation compared to $c(\underline{KY})_4$ assemblies (Figure 4b). Quantitatively, for the same water uptake level, the conductivity of the $c(\underline{KF})_4$ assembly surpasses that of the $c(\underline{KY})_4$ assembly by two orders of magnitude, dropping to a difference of one order of magnitude with increased water uptake. This behavior suggests that excess water molecules that bind to the phenol groups in the $c(\underline{KY})_4$ assembly do not actively contribute to proton transport pathways. Interestingly, superior conductivity is observed for $c(\underline{KF})_4$ upon full hydration, which can be attributed to the larger amount of hydrogen bonds between water molecules, and between water molecules and peptide side chains and TFA ions, in the channel indicated by the simulations (Figure S12, Supporting Information), probably due to stronger confinement to the channel by the more hydrophobic aromatic periphery provided by phenylalanine, similar to that of high-performance polyelectrolytes, such as Nafion.[52,53]

5. Proton Transport Mechanisms

More detailed insight into the effect of hydration on proton transport processes in the assemblies was obtained from the loss tangent (tan ϕ) dielectric response (extracted as the ratio between the real and imaginary impedance; upper inset in Figure 4a).[54] For both assemblies, the tan ϕ curve was bell-shaped when plotted on a logarithmic scale. With increasing relative humidity, the curve shifted to higher frequencies, indicating a decrease in the

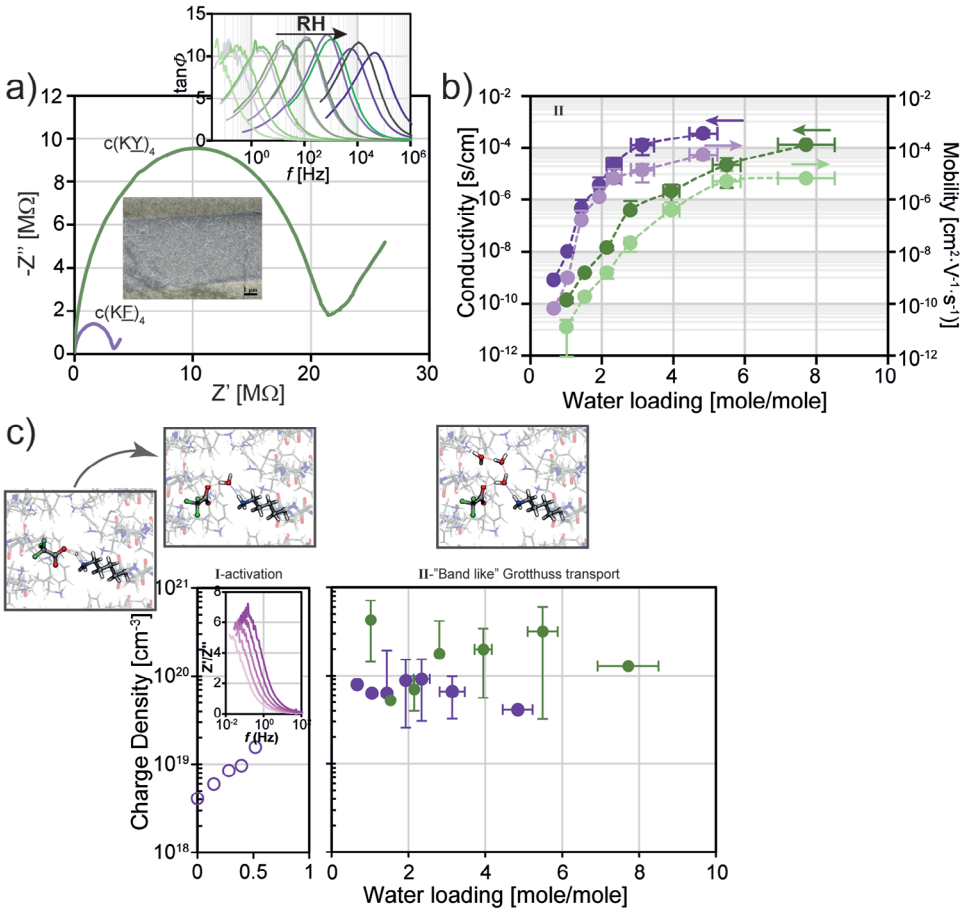

Figure 4. Electrical characteristics of $c(\underline{KF})_4$ and $c(\underline{KY})_4$ assemblies as function of hydration. a) Nyquist plots of the electrical impedance (IS) of $c(\underline{KF})_4$ (purple) and $c(\underline{KY})_4$ (green) films at 60% RH. A scanning electron microscopy (SEM) image of a $c(\underline{KF})_4$ film between the electrodes is presented in the lower inset. IS data at 10–80% RH with a ramp of 10% are provided as loss tangent spectra in the upper inset, where the loss tangent is calculated as $tan\ (\phi) = -\frac{Z'}{Z''}$. The corresponding Nyquist plots are provided in Figure S13 (Supporting Information). This data was collected in parallel to the hydration data in Figure 3. b) Conductivity (dark color tone) and mobility (light color tone) of $c(\underline{KF})_4$ (purple) and $c(\underline{KY})_4$ (green) in region II as functions of hydration. Conductivity was obtained from the relationship $\sigma = L/RA$, where R is the resistance, extracted as the diameter of the semicircle in the Nyquist plots, L is the distance between the electrodes (20 µm), and A is the cross-section of the film between the IDE electrodes (14.4×10^{-6} cm^2). Mobility was obtained from loss tangent curves using Equation (1). c) charge carrier density as a function of water uptake in regions I and II. Charge carrier concentration was obtained from the relationship $[C] = \sigma/e\mu$. IS data in region I is presented in the inset as loss tangent spectra. Illustrations of salt-bridge hydration leading to proton activation (dominant in range I) and to the formation of water wires are presented at the top of the panel.

relaxation time. The frequency at which tanϕ maximizes, f_{max}, was used to evaluate the proton mobility, $\mu_{p,}$ according to the relationship.[54]

$$\mu_p = \frac{2\pi f_{max}}{kT} \cdot \left(\frac{L}{2tan\phi_{max}}\right)^2 \quad (1)$$

where L is the gap between the two contacts, k is the Boltzmann constant, and T is the temperature. For both peptide assemblies, the mobility was found to follow similar trends to the conductivity with respect to changes in hydration (Figure 4b), namely, mobility increased exponentially at low hydration levels and saturated at higher hydration levels, in similarity to the conductivity behavior. An analogous dependence on hydration was also observed for Nafion.[55] Since the conductivity is proportional to the product of the charge carrier concentration and the mobility, these results indicate that variations in the conductivity with relative humidity originate mainly from changes in the mobility of the charge carriers. Indeed, the charge carrier density, evaluated using the relation $[C] = \sigma/e\mu$ (where σ is the conductivity and μ is the mobility of the charge carriers), was found to be $\approx 10^{20}$ cm^{-3} throughout hydration range II for both assemblies (Figure 4c). Notably, these results indicate that the overall higher conductivity observed for the $c(\underline{KF})_4$ assembly derives from a higher charge carrier mobility, despite its lower water absorption. The charge carrier density magnitude was found to be comparable to the molecular density of the TFA anions in the film, which was obtained from the relationship $n_{TFA} = \frac{2m_{pep\cdot 2TFA}}{M_{pep\cdot 2TFA} \times t}$, where $m_{pep\cdot 2TFA}$ is the mass density of the peptide-TFA salt determined with a quartz crystal microbalance (QCM), $M_{pep\cdot 2TFA}$ is its molecular weight, and t is the film thickness (found by profilometry measurements to be ≈460 nm). The similar charge and TFA densities in the film suggests that

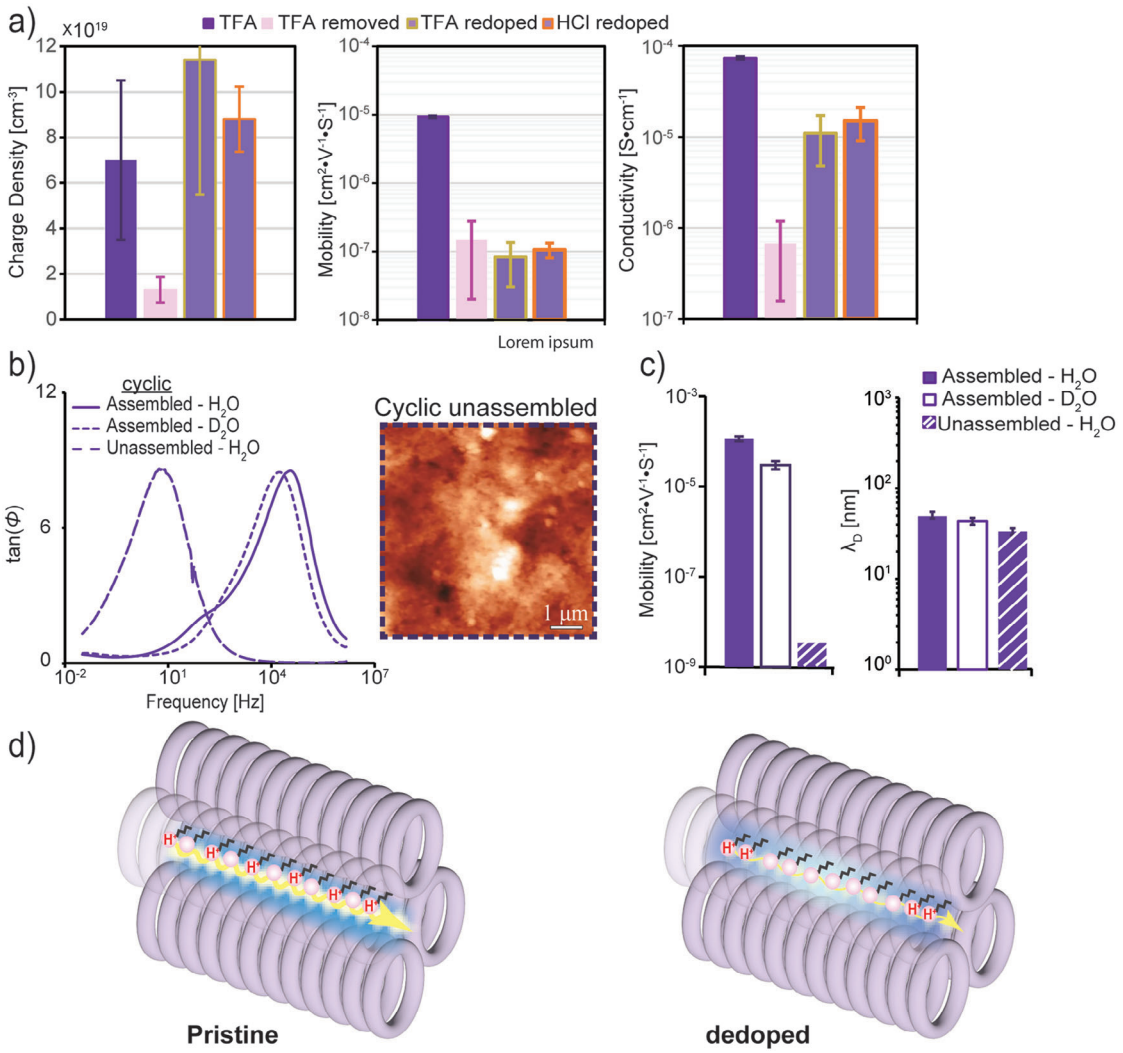

Figure 5. Effects of counterion and order on charge transport. a) Counterion effects: Charge carrier density, mobility, and conductivity of c(KF)$_4$ films in the pristine state, after TFA counterion removal and after "redoping". "Redoping" was performed by exposure of the c(KF)$_4$ film to TFA or HCl vapor. b) Self-assembly effects: loss tangent curves of assemblies of c(KF)$_4$ in H_2O and D_2O environments and of a film of non-assembled c(KF)$_4$. Experiments were conducted under 70% RH. An AFM image of the unassembled cyclic peptide is shown on the right. c) Mobility of the charge carriers and Debye screening length of c(KF)$_4$ films (inversely proportional to the square of the charge carrier concentration) obtained from the loss tangent curves in b). Data in pannels (a–d) represents three replicas at least. d) Schematic representation of the suggested model for charge transport in the interstitial channels in the presence of TFA (pristine) and without TFA (de-doped).

TFA anions are the source of the charge carriers. Indeed, a decrease of almost an order of magnitude in the concentration of charge carriers was observed upon the removal of the TFA ions (**Figure** 5a), in line with the order of magnitude reduction in the concentration of anions in the sample (Table S2, Supporting Information). Charge carrier density was restored by a "redoping" process, in which the sample was exposed to TFA or HCl vapor (Figure 5a). In both cases, F/Cl atoms were re-incorporated into the film (Table S2, Supporting Information), and the ammonium peak in the XPS N1s binding energy range was recovered (Figure S14, Supporting Information). We note that the XRD spectra and AFM images indicated that the long-range order and morphology of the structure were preserved during the vapor exposure process (Figures S7 and S15, Supporting Information, respectively). Interestingly, despite of somewhat higher water absorption in the case of Cl ions (Figure S16, Supporting Information) similar electrical behavior was observed for the system regardless of the type of counter ions used for redoping. Indeed, MD simulations indicated a similar behavior for the two types of ions, with the counter ions incorporated in the channels forming salt bridge with lysine side chains (Figure 2; Figure S17, Supporting Information).

While the counter ions appear to be the source of charge carriers, the fact that the behavior of the system was similar regardless of the type of counter ions indicated that the same type of charge carrier is formed in the system in both cases. The participation of protons, and not the counterions, in the charge transport process, was confirmed by kinetic isotope effect experiments that indicated a decrease in the mobility of the charge carriers in the presence of D_2O vapor (Figure 5b,c). We therefore

conclude that the counterions serve as proton dopants. This phenomenon aligns with the simulations, which showed that the anions are immobile (Figure 1d). Notably, our results suggest that even though the peptides are cationic, the predominant charge carriers are protons and not the hydroxide ions usually considered to be the charge carriers in such cationic systems.[56]

Support for the doping mechanism may be derived from the increase in the charge carrier concentration in range I of hydration (Figure 4c). The increase in charge carrier concentration in hydration range I was reflected by an increase in $tan\varnothing_{max}$, which reached a constant value in range II (compared in the insets of Figure 4c and a, respectively). In range I, the hydration process facilitates the transition of protons from a bound state to a solvated state in which they can readily translocate through hydrogen bonded chains in the system. This process can be considered analogous to the thermal activation of dopants in semiconductors in the freeze-out range. The simulations provided support for this "dopant activation" process: without water molecules protons were tethered to the salt bridges between lysine and TFA and were relatively immobile (inset of Figure 4c), upon hydration, water molecules interacted with the salt bridges, forming hydrogen bonded chains that include TFA anions and the lysine side chains (inset of Figure 4c; Figure S12, Supporting Information). This interaction awards mobility to the salt-bridge protons. Notably, the charge activation process occurs exclusively in the interstitial channels and not in the lumens of the nanotubes. As a result, the contribution of the lumens to proton conductivity is deemed negligible.

Once mobilized, protons, whose concentration is dictated by the concentration of the salt bridge bonds in the channels, could be transported along hydrogen bonded chains throughout the length of the nanochannels (Figure 5d) in processes resembling the proton transfer mechanisms observed in biological proton channels. The rate at which protons are transferred is dictated by the amount of water molecules in the channel. Hence, in analogy to semiconductor doping, in terms of proton concentration, hydration range II can be regarded as an "extrinsic range." As noted above, the proton mobility of the $c(\underline{KF})_4$ assembly was found to be higher than that of the $c(\underline{KY})_4$ assembly, with proton mobility exceeding values of 5×10^{-5} and 7×10^{-6} $cm^2\ V^{-1}\ s^{-1}$ at saturation for $c(\underline{KF})_4$ and $c(\underline{KY})_4$, respectively, Figure 5b). These proton mobility values represent diffusion coefficient larger than that of water self-diffusion, indicating charge transfer by the Grotthuss mechanism. Importantly, these mobility values represent diffusion coefficients that are similar to those measured in natural proton channels.[2,57] Remarkably, because of the highly ordered hierarchical assembly, efficient proton transport can proceed over extremely long distances. It should be mentioned that the mobility values in the peptide system are of the same order of magnitude as those measured for Nafion thin films.[58] This is probably due to a similar conduction mechanism, which is controlled by the containment of proton transport to nanometric water channels sheathed within hydrophobic domains.[55] Evidence for the importance of channel formation for proton conductivity was obtained by comparing the behavior of $c(\underline{KF})_4$ assemblies to that of films of non-assembled peptides (Figure 5b,c). Values of $\tan(\phi)_{max}$ were found to be similar in the two cases, indicating similar charge carrier concentrations, as expected. However, proton mobility decreased by about four orders of magnitude for the non-assembled peptide films, indicating the importance of the hierarchical assembly in attaining a high proton transfer rate.

In addition to the doping effect, counterions were also found to affect proton mobility. For example, for $c(\underline{KF})_4$ the reduction in charge carrier concentration upon TFA removal was accompanied by a drop of almost two orders of magnitude in their mobility (Figure 5a), despite the fact that the order and morphology of the films were retained (Figure 2d; Figure S7, Table S1, Supporting Information), indicating that the interstitial channel structure was not affected by removal of the counterions. As explained above, removal of the counterions was accompanied by both a reduced hydration level Figure 3b) and an increase in the quantity of water-lysine hydrogen bonds at the expense of hydrogen bonds involving TFA anions (Figure S12, Supporting Information). Thus, it can be concluded that the counterions influence proton mobility through their control over the hydrogen bond networks in the system. Interestingly, proton mobility did not recover during the "redoping" process (Figure 5a). This behavior may be attributed to chemical degradation, which is manifested by the broadening of the XPS N1S peak (Figure S12, Supporting Information).

6. Conclusion

This study introduces a straightforward peptide design capable of encoding essential folding information that facilitates the formation of nanochannels supporting highly effective proton transport over tens of micrometers. The cyclic octa peptides employed, characterized by a fourfold symmetry and the incorporation of an amphiphilic dipeptide unit, undergo hierarchical self-assembly, resulting in the formation of extended hydrophilic nanochannels featuring titratable side chains. The hydration of these nanochannels facilitates proton transport along the nanochannels via hydrogen bonded chains, with proton transfer rates akin to those observed in transmembrane protein channels across macroscale distances, occurring by the Grotthuss mechanism. Additionally, an acid doping mechanism facilitates precise control of both the concentration and the translocation rate of protons in the channels. This study thus provides a breakthrough in the integration of charge transport mechanisms that occur in biological systems over nanometric distances into microscale systems, establishing the foundation for the creation of innovative functional materials based on peptide assemblies. Our findings underscore the pivotal role played by hierarchical assembly of the peptides in determining their functional behavior. Notably, the performance of these hierarchical assembled materials aligns with that of state-of-the-art materials used in polyelectrolyte membranes.[59] Moreover, the peptides' design flexibility offers ample opportunity to further improve the functional behavior of these assemblies.[20,22,27] The bioinspired materials studied here, which are characterized by inherent environmental friendliness and biocompatibility, hold tremendous promise for diverse applications, ranging from energy to bioelectronics.

7. Experimental Section

Peptide Synthesis: Peptides were synthesized on a 2-chlorotrytyl chloride resin by using Fmoc-based solid phase synthesis protocols. Peptides

were cleaved from the resin in a 1:1:3 mixture of acetic acid (Bio-Lab), trifluoroethanol (Sigma Aldrich), and dichloromethane (DCM; Bio-Lab) for 2 h at ambient temperature, followed by washing three times in DCM. The side-chain-protected linear peptides were cyclized by utilizing PyBOP (Sigma Aldrich) as the coupling agent. Thereafter, a side chain deprotection step was performed in a 95:2.5:2.5 mixture of trifluoroacetic acid (TFA; Bio-Lab), triisopropylsilane (Sigma Aldrich), and triply distilled water (TDW). The synthesized cyclic peptides were purified by HPLC, and their molecular weights were determined by LC-MS. Peptides with a purity above 95% were used.

Self-Assembly: Peptide self-assembly was facilitated by dissolving the peptide powders in TDW to which acetonitrile (ACN; J.T. Baker) was added to yield a 10:90 TDW:ACN solution (1 mM). Samples were equilibrated in closed Eppendorf tubes for two weeks at room temperature.

TFA was removed by adding NH_4OH (0.3%) to the self-assembled peptide solution in a 1:9 volumetric ratio of NH_4OH to peptide solution. After 2 h of incubation, the solution was drop-cast and left to dry. The dried films were dipped into 0.3% NH_4OH solution, and the samples were used for further analysis and characterization after drying.

"Redoping" of the samples with counterions was achieved by exposing the TFA-removed film to TFA or HCl vapors for 1 min at 10-s intervals.

X-ray diffractometry (XRD) was performed on samples prepared by drop casting 10–20 µL of peptide solution onto glass coverslips precleaned with piranha solution [1:3 30% hydrogen peroxide (J.T. Baker):96% sulfuric acid (Bio-Lab)]. X-ray diffractometry of the samples was performed on a Panalytical Empyrean III multipurpose diffractometer (CuKα radiation, λ = 1.541 Å) equipped with a pixCEL^{3D} detector in 0D (position-sensitive) open-detector mode and with an X-ray tube operated at v = 45 kV, I = 40 mA. The instrument was fitted with Panalytical Multi-Core automated optics and a 3-axis Eulerian (χ-ϕ-z) cradle for fine sample alignment. Each sample was mounted on a zero-background pure Si plate, which was placed directly on the Eulerian cradle. Measurements were conducted in reflectance mode ($\theta/2\theta$) between 3.0° and 25.0° 2θ. A beam knife was used to reduce air-scattering from the direct beam at low angles. Diffractograms were obtained at multiple orientations to the incident beam (ϕ), confirming the presence of multiple low-angle peaks. Measurements were also collected in grazing incidence geometry (GIXD) in which the incident angle of the X-ray beam was held constant at 0.3°.

X-ray photoelectron spectroscopy (XPS) was conducted with an ESCALAB Xi+ spectrometer with an Al Kα source and a 500-µm spot size (Thermo Fisher Scientific, USA) on samples prepared by drop casting 2 µL of peptide solutions (1 mM) on piranha-cleaned silicon substrates. XPS survey spectra were calibrated with respect to the C1s binding energy peak (284.84 eV). High-resolution spectra were obtained with an analyzer bandpass of 20 eV. The chemical composition of the peptides was verified by the atomic percentage of the C1s and N1s peaks. The presence of TFA was confirmed and evaluated by using the F1s peak. The ratio between protonated and non-protonated amines was extrapolated from the N1s scan peaks at 401.7 and 399.9 eV for protonated and non-protonated amines, respectively.

Cryo-electron microscopy (cryo-EM) was performed on samples prepared by depositing 3 µL of solution of c(K$\underline{F}$)$_4$ assemblies (1 mM) on glow discharged Quantifoil R 1.2/1.3 holey carbon grids (Quantifoil Micro Tools GmbH, Germany). Samples were blotted manually, washed with 5 µL of doubly distilled water, and then blotted again for 3 s at room temperature, followed by vitrification by rapidly plunging them into liquid ethane with an in-house-built plunging apparatus. The frozen samples were stored in liquid nitrogen until imaging. For imaging, the samples were loaded under cryogenic conditions and imaged in low-dose mode on a Glacios microscope (Thermo-Fisher) operated at 200 kV. Automated data collection was performed using EPU (Thermo-Fisher). Movies were collected at a calibrated pixel size of 0.89 Å by a Falcon4i direct electron detector fitted behind a Selectris X energy filter (Thermo-Fisher) set to ±5 eV around the zero-loss peak. The detector was operated in a dose fractionated counting mode, at a dose rate of 8 ē•pixel^{-1}•s^{-1}, with total electron dose of 30 $\bar{e}$•Å^{-2}. Data was collected in a defocus range of −0.5 to −1.5 µm. All processing was performed using cryoSPARC v4.3.0.[60] Dose-fractionated movie stacks were patch-motion corrected, and their defocus values were estimated. The aligned sum images were used for further processing. Particles were picked using a filament tracer, followed by extraction of 256-Å long overlapping segments (with a shift of twice the expected axial rise). 2D class averages were manually selected and used for further 3D refinement. All selected classes had clear signatures of a striated pattern. Ab-initio reconstruction of three classes was used to prepare initial maps for further refinement. A clear four-tube class was selected for further refinement of the fourfold hierarchically assembled nanotubes. Helical refinement with an expected 90° twist and 10 Å rise was used to reconstruct the final 3D map.

Atomic force microscopy (AFM) images were obtained for samples prepared on silicon substrates with a 100-nm thick thermal oxide. Prior to deposition of the peptide solution, the substrates were cleaned with fresh piranha solution for 30 min. The morphology of the self-assembled films was imaged using either a Solver-Pro AFM (NT-MDT, Russia) or a CoreAFM (Nanosurf, Switzerland), in tapping mode using non-contact tips with a spring constant of 3 N•m^{-1} and 75 kHz resonance frequency (Multi75Al-G, BudgetSensors, Bulgaria). Topography images were processed for first-order polynomial fit plane subtraction. The AFM software was also used for cross-section analysis, from which the nanotube diameter was obtained.

High-resolution scanning electron microscopy (HRSEM) images were obtained for peptide films deposited on interdigitated electrode (IDE) electrodes as described below (Verios 460, Thermo Fisher Scientific, USA). To achieve high-quality images, 0.5 mM solutions were used. Images were captured with a through-the-lens (TLD) detector using a secondary electron mode.

Profilometry measurements to extract the peptide film thickness were obtained with a device used for electrical measurements (Dektak 150, Veeco Instruments, USA). The film was scratched with a surgical knife at the edges of the IDE, and the scratched area was used as a baseline for the measurement. The film thickness was determined as the average of three measured cross-sections across the electrode pair.

Hydration experiments were conducted with a quartz crystal microbalance (QCM) with a dissipation monitoring system (QCM-D, openQCM Q-1, Italy) and 5 MHz AT-cut quartz crystals with gold electrodes (Qsense, Novatech, Italy). QCM samples were cleaned by consecutive sonication in acetone, methanol, and isopropanol (Bio-Lab) for 15 min each. Prior to peptide film deposition, freshly cleaned crystals were placed in a closed environment under a dry nitrogen flow (99.99%) for 1 h, and their resonance frequency was measured using the 3rd overtone. Thereafter, 10 µL peptide solution (1 mM) was drop-cast on the quartz chip and left to dry overnight under ambient conditions. The mass density of the peptides was calculated, using the Sauerbrey equation, from differences in the resonance frequency between a freshly cleaned chip and a chip covered with the peptide film under dry nitrogen flow, as follows:[61]

$$m_{pept} = -C \cdot \frac{\Delta f}{n} \tag{2}$$

where C is the mass sensitivity constant, taken as 17.7 ng•cm^{-2} for the 5 MHz AT-cut quartz crystals,[61] n is an integer representing the overtone measured, i.e., 3, and Δf is the change in resonance frequency. The molar density of the peptides on the surface of the chip was calculated by dividing the calculated mass by the molar weight of the relevant peptide. Molar densities of ≈15 nM cm^{-2} were obtained, which (by taking into account the area of the film deposited on the QCM sensor) corresponds to an estimated amount of 11 nM of the peptide, as expected based on the concentration of the peptide in solution and the drop cast volume on the QCM. Following peptide deposition, absorption measurements were obtained by monitoring the QCM resonance frequency while controlling the relative humidity of the chamber using an automated humidity generation system (NEXTRON, South Korea and RH-200, L&C Science and Technology, USA). The Sauerbrey model (Equation 2) was used to derive the mass of water absorbed onto the sample.[61,62] Negligible changes in the dissipation of the samples, which were monitored in parallel for the entire relative humidity range, validated the films' rigid coupling and hence the suitability of the Sauerbrey model for analyzing the data. The measurements were replicated (×5 for c(K$\underline{F}$)$_4$ and ×3 for c(K$\underline{Y}$)$_4$),

except in the range of 0 to 10% RH, for which only one measurement was made.

Electrical characterizations were performed on gold IDE chips fabricated on glass substrates (Unit for Nanofabrication, The Hebrew University of Jerusalem, Israel). IDEs with 5-, 10-, 15-, 20-, and 25-µm spacings and a constant contact length of 3.2 cm were used. Prior to peptide film deposition, the IDE chips were thoroughly cleaned by sonication in ethanol, methanol, and isopropanol for 15 min each. Next, the samples were silanized by introducing 50 µL of hexamethyldisilane (HMDS; Sigma-Aldrich) onto the chip surface in a closed petri dish placed on a 90-°C pre-heated hot plate for 15–30 min to prevent parasitic contribution of the substrates' hydroxyl groups. Excess HMDS was then washed away by sonicating the samples in isopropanol for 5 min, and the chips were dried under dry nitrogen flow and cured in an oven at 110 °C for 30 min. Each device was prepared by three to four consecutive steps of drop casting a 2-µL drop of the peptide solution on the IDE and drying. Impedance spectroscopy (IS) measurements were performed in a probe station (MPS-PTH, NEXTRON, South Korea) in a two-probe configuration using a frequency response analyzer and a dielectric interface (1260b & 1296, Solartron Metrology, UK). Spectra were recorded over a frequency range of 32 mHz to 3.2 MHz, using AC voltage with a 100-mV AC amplitude and a 0-V DC component. The bulk resistance, R, of the peptide films was obtained by fitting the semi-circle regime in the impedance spectra using a custom-made MATLAB script. The conductivity of the film was extracted as $\sigma = \frac{L}{RA}$, where A is the contact cross section and L, the gap distance. All experiments presented in the manuscript were repeated at least three times. Averaged data is presented with the error calculated as the standard deviation.

Molecular Dynamics (MD) Simulations: MD simulations were performed using the Sander and Pmemd.cude programs from the AMBER suite code,[63,64] which were employed successfully in previous studies for biomolecular systems (see, e.g., refs. [65–67]). In the present work, ff19SB force field[68] and the TIP3P water model[69] were used. A Langevin thermostat with a collision frequency of 5 ps^{-1} was employed. The TFA interactions were parametrized using the Antechamber and Parmchk2 programs, both included in the AMBER suite. The preparation of the system and stability checks are described in the Supporting Information. The post-analysis of the MD trajectories was conducted using a combination of the own developed code and the Python library MDTraj.[70]

The initial coordinates of a cyclic peptide stack were extracted from electron diffraction data obtained for crystals of similar cyclic peptide molecules (c(AF)$_4$, courtesy of Prof. Ghadiri at the Scripps Research Institute), and were matched to the current design.[27] The MD simulations were conducted either for a system comprising four peptide nanotubes, each consisting of a stack of ten cyclic peptides in a fully hydrated environment, or for a periodic assembly of peptide nanotubes, as follows.

Hydrated Four-Peptide Nanotubes: The four nanotubes were placed parallel to each other in a periodic cuboid box of side lengths ranging from 80 to 90 Å filled with ≈13 000 water molecules. Simulations were performed for different proportions of protonated versus neutral lysine groups. The charge neutrality of the system was maintained by introducing the corresponding amount of negatively charged TFA^- (or Cl^-) ions in the system. After the system had been properly prepared (see Supporting Information), the behavior of the system was studied by performing free MD simulations at T = 300 K, for a total simulation time of 100 ns.

Periodic assembly simulations (simulation time 100 ns) were performed for a unit cell containing four stacks of eight cyclic peptides, with periodicity in three (x,y,z) directions. The cuboid unit cell dimensions (≈40 × 40 × 40 $Å^3$) were adjusted using NPT conditions (P = 1 atm and T = 300 K). This approach allowed to control the number of water molecules (0, 1, 2, 3, 4, and 5 water molecules per peptide) in the intra- and inter-channels. Simulations were obtained both for the case of neutral amines of the lysine groups (0% protonation), and for the system with half of the amines protonated (50% protonation) but with charge neutrality. In the 50% protonation case, charge neutrality was maintained by including the appropriate amount of TFA^- counterions in the interstitial channels. Diffusion coefficients of water molecules and TFA ions were calculated using the slope of the mean squared displacement as a function of time, MSD(t).

Supporting Information

Supporting Information is available from the Wiley Online Library or from the author.

Acknowledgements

S.C., J.V.M., and O.S. contributed equally to this work. This research was supported by the Israel Science Foundation – Personal grants (Grants No. 375/18 and 1654/22) and FIRST Program (grant No. 2527/20) and by a Collaboration grant of the Ilse Katz Institute for Nanoscale Science and Technology. The authors acknowledge the financial support of the Spanish Ministry of Science and Innovation through project no. PID2021-125604NB, and through the "María de Maeztu" Programme for Units of Excellence in R&D (CEX2023-001316-M). O.S. was supported by the Kreitman Hightech/Biotech/Chemtech fellowship. S.M.M.R. was supported by the BGU Kreitman School post-doctorate fellowship. Devices were fabricated at the Unit for Nanofabrication of The Hebrew University of Jerusalem. The authors are grateful to Prof. M. Reza Ghadiri and Dr. Luke J. Leman for supplying the initial coordinates of the model peptides, and to the Guzik Foundation for the generous support of the BGU's Cryo-electron microscopy unit.

Conflict of Interest

The authors declare no conflict of interest.

Data Availability Statement

The data that support the findings of this study are available from the corresponding author upon reasonable request.

Keywords

molecular dynamic simulations, peptides, proton channels, proton transport, self-assembly

Received: June 28, 2024
Revised: October 1, 2024
Published online: November 12, 2024

[1] T. E. Decoursey, *Physiol. Rev.* **2003**, *83*, 475.
[2] T. E. Decoursey, *Physiol. Rev.* **2013**, *93*, 599.
[3] J. F. Nagle, S. Tristram-Nagle, *J. Membr. Biol.* **1983**, *74*, 1.
[4] W. Gu, V. Helms, *J. Am. Chem. Soc.* **2009**, *131*, 2080.
[5] A.-N. Bondar, H. Dau, *Biochim. Biophys. Acta – Bioenerg.* **2012**, *1817*, 1177.
[6] M. Tagliazucchi, I. Szleifer, *Mater. Today* **2015**, *18*, 131.
[7] I.-M. Andrei, M. Barboiu, *Biomolecules* **2022**, *12*, 1473.
[8] S.-P. Zheng, L.-B. Huang, Z. Sun, M. Barboiu, *Angew. Chem., Int. Ed.* **2021**, *60*, 566.
[9] M. Barboiu, A. Gilles, *Acc. Chem. Res.* **2013**, *46*, 2814.
[10] F. Otis, M. Auger, N. Voyer, *Acc. Chem. Res.* **2013**, *46*, 2934.
[11] J. D. Lear, Z. R. Wasserman, W. F. DeGrado, *Science* **1988**, *240*, 1177.
[12] L. Wu, Z. Zhang, J. Ran, D. Zhou, C. Li, T. Xu, *Phys. Chem. Chem. Phys.* **2013**, *15*, 4870.

[13] D. W. Shin, M. D. Guiver, Y. M. Lee, *Chem. Rev.* **2017**, *117*, 4759.
[14] Y. Sun, J. Wei, Z. Fu, M. Zhang, S. Zhao, G. Xu, C. Li, J. Zhang, T. Zhou, *Adv. Mater.* **2023**, *35*, 2208625.
[15] N. Amdursky, E. D. Głowacki, P. Meredith, *Adv. Mater.* **2019**, *31*, 1802221.
[16] M. Jia, J. Kim, T. Nguyen, T. Duong, M. Rolandi, *Biopolymers* **2021**, *112*, e23433.
[17] S. Mondal, Y. Agam, R. Nandi, N. Amdursky, *Chem. Sci.* **2020**, *11*, 3547.
[18] D. D. Ordinario, L. Phan, W. G. WalkupIV, J.-M. Jocson, E. Karshalev, N. Hüsken, A. A. Gorodetsky, *Nat. Chem.* **2014**, *6*, 596.
[19] M. Amit, S. Appel, R. Cohen, G. Cheng, I. W. Hamley, N. Ashkenasy, *Adv. Funct. Mater.* **2014**, *24*, 5873.
[20] O. Silberbush, M. Amit, S. Roy, N. Ashkenasy, *Adv. Funct. Mater.* **2017**, *27*, 1604624.
[21] J. Lee, I. R. Choe, Y.-O. Kim, S. D. Namgung, K. Jin, H.-Y. Ahn, T. Sung, J.-Y. Kwon, Y.-S. Lee, K. T. Nam, *Adv. Funct. Mater.* **2017**, *27*, 1702185.
[22] C. Ma, J. Dong, M. Viviani, I. Tulini, N. Pontillo, S. Maity, Y. Zhou, W. H. Roos, K. Liu, A. Herrmann, G. Portale, *Sci. Adv.* **2020**, *6*, eabc0810.
[23] H. Semizo, R. Yabu, Y. Ohgishi, H. Kai, H. Nishimura, Y. Matsuo, *Bioengineering* **2023**, *10*, 1223.
[24] H. Semizo, R. Yabu, H. Kai, Y. Ohgishi, Y. Matsuo, *Chem. Phys.* **2023**, *573*, 112022.
[25] S. M. M. Reddy, E. Raßlenberg, S. Sloan-Dennison, T. Hesketh, O. Silberbush, T. Tuttle, E. Smith, D. Graham, K. Faulds, R. V. Ulijn, N. Ashkenasy, A. Lampel, *Adv. Mater.* **2020**, *32*, 2003511.
[26] J. Lerner Yardeni, M. Amit, G. Ashkenasy, N. Ashkenasy, *Nanoscale* **2016**, *8*, 2358.
[27] S. Roy, L. Zheng, O. Silberbush, M. Engel, Y. Atsmon-Raz, Y. Miller, A. Migliore, D. N. Beratan, N. Ashkenasy, *J. Phys. Chem. B* **2021**, *125*, 12741.
[28] O. Silberbush, M. Engel, I. Sivron, S. Roy, N. Ashkenasy, *J. Phys. Chem. B* **2019**, *123*, 9882.
[29] M. R. Ghadiri, J. R. Granja, R. A. Milligan, D. E. McRee, N. Khazanovich, *Nature* **1993**, *366*, 324.
[30] R. J. Brea, C. Reiriz, J. R. Granja, *Chem. Soc. Rev.* **2010**, *39*, 1448.
[31] J. D. Hartgerink, J. R. Granja, R. A. Milligan, M. R. Ghadiri, *J. Am. Chem. Soc.* **1996**, *118*, 43.
[32] J. Montenegro, M. R. Ghadiri, J. R. Granja, *Acc. Chem. Res.* **2013**, *46*, 2955.
[33] M. R. Ghadiri, J. R. Granja, L. K. Buehler, *Nature* **1994**, *369*, 301.
[34] M. Calvelo, C. I. Lynch, J. R. Granja, M. S. P. Sansom, R. Garcia-Fandiño, *ACS Nano* **2021**, *15*, 7053.
[35] R. García-Fandiño, M. Amorín, L. Castedo, J. R. Granja, *Chem. Sci.* **2012**, *3*, 3280.
[36] R. García-Fandiño, J. R. Granja, M. D'Abramo, M. Orozco, *J. Am. Chem. Soc.* **2009**, *131*, 15678.
[37] J. Comer, F. Dehez, W. Cai, C. Chipot, *J. Phys. Chem. C* **2013**, *117*, 26797.
[38] P. S. Zelenovskiy, E. M. Domingues, V. Slabov, S. Kopyl, V. L. Ugolkov, F. M. L. Figueiredo, A. L. Kholkin, *ACS Appl. Mater. Interfaces* **2020**, *12*, 27485.
[39] P. Zelenovskii, M. Soares, C. Bornes, I. Marin-Montesinos, M. Sardo, S. Kopyl, A. Kholkin, L. Mafra, F. Figueiredo, *Nat. Commun.* **2024**, *15*, 5516.
[40] H. R. Saibil, *Mol. Cell* **2022**, *82*, 274.
[41] X. C. Bai, G. McMullan, S. H. W. Scheres, *Trends Biochem. Sci* **2015**, *40*, 49.
[42] F. Wang, O. Gnewou, C. Modlin, L. C. Beltran, C. Xu, Z. Su, P. Juneja, G. Grigoryan, E. H. Egelman, V. P. Conticello, *Nat. Commun.* **2021**, *12*, 407.
[43] E. H. Egelman, *Curr. Opin. Struct. Biol.* **2024**, *85*, 102788.
[44] L. T. Yu, M. C. Hancu, M. A. B. Kreutzberger, A. Henrickson, B. Demeler, E. H. Egelman, J. D. Hartgerink, *J. Am. Chem. Soc.* **2023**, *145*, 5285.
[45] X. C. Bai, G. McMullan, S. H. Scheres, *Trends Biochem. Sci.* **2015**, *40*, 49.
[46] F. Wang, O. Gnewou, S. Wang, T. Osinski, X. Zuo, E. H. Egelman, V. P. Conticello, *Matter* **2021**, *4*, 3217.
[47] M. A. B. Kreutzberger, S. Wang, L. C. Beltran, A. Tuachi, X. Zuo, E. H. Egelman, V. P. Conticello, *Proc. Natl. Acad. Sci. USA* **2022**, *119*, 2121586119.
[48] L. Pieri, F. Wang, A.-A. Arteni, M. Vos, J.-M. Winter, M.-H. Le Du, F. Artzner, F. Gobeaux, P. Legrand, Y. Boulard, S. Bressanelli, E. H. Egelman, M. Paternostre, *Proc. Natl. Acad. Sci. USA* **2022**, *119*, 2120346119.
[49] E. F. Pettersen, T. D. Goddard, C. C. Huang, G. S. Couch, D. M. Greenblatt, E. C. Meng, T. E. Ferrin, *J. Comput. Chem.* **2004**, *25*, 1605.
[50] D. J. Rubin, S. Amini, F. Zhou, H. Su, A. Miserez, N. S. Joshi, *ACS Nano* **2015**, *9*, 3360.
[51] D. G. Isom, C. A. Castañeda, B. R. Cannon, B. García-Moreno E, *Proc. Natl. Acad. Sci. USA* **2011**, *108*, 5260.
[52] K. Schmidt-Rohr, Q. Chen, *Nat. Mater.* **2008**, *7*, 75.
[53] K. A. Mauritz, R. B. Moore, *Chem. Rev.* **2004**, *104*, 4535.
[54] T. Q. Nguyen, C. Breitkopf, *J. Electrochem. Soc.* **2018**, *165*, E826.
[55] S. Ochi, O. Kamishima, J. Mizusaki, J. Kawamura, *Solid State Ion* **2009**, *180*, 580.
[56] C. Zhong, Y. Deng, A. F. Roudsari, A. Kapetanovic, M. Anantram, M. Rolandi, *Nat. Commun.* **2011**, *2*, 476.
[57] C. A. Wraight, *Biochim. Biophys. Acta – Bioenerg.* **2006**, *1757*, 886.
[58] O. Sel, L. To Thi Kim, C. Debiemme-Chouvy, C. Gabrielli, C. Laberty-Robert, H. Perrot, *Langmuir* **2013**, *29*, 13655.
[59] C. Yin, J. Li, Y. Zhou, H. Zhang, P. Fang, C. He, *ACS Appl. Mater. Interfaces* **2018**, *10*, 14026.
[60] A. Punjani, J. L. Rubinstein, D. J. Fleet, M. A. Brubaker, *Nat. Methods* **2017**, *14*, 290.
[61] X. Huang, Q. Bai, J. Hu, D. Hou, *Sensors* **2017**, *17*, 1785.
[62] A. Alassi, M. Benammar, D. Brett, *Sensors* **2017**, *17*, 2799.
[63] D. A. Case, H. M. Aktulga, K. Belfon, I. Y. Ben-Shalom, J. T. Berryman, S. R. Brozell, D. S. Cerutti, T. E. Cheatham III, G. A. Cisneros, V. W. D. Cruzeiro, T. A. Darden, N. Forouzesh, G. Giambaşu, T. Giese, M. K. Gilson, H. Gohlke, A. W. Goetz, J. Harris, S. Izadi, S. A. Izmailov, K. Kasavajhala, M. C. Kaymak, E. King, A. Kovalenko, T. Kurtzman, T. S. Lee, P. Li, C. Lin, J. Liu, T. Luchko, et al., in *Amber 2023*, University of California, San Francisco, **2023**.
[64] D. A. Case, H. M. Aktulga, K. Belfon, D. S. Cerutti, G. A. Cisneros, V. W. D. Cruzeiro, N. Forouzesh, T. J. Giese, A. W. Götz, H. Gohlke, S. Izadi, K. Kasavajhala, M. C. Kaymak, E. King, T. Kurtzman, T.-S. Lee, P. Li, J. Liu, T. Luchko, R. Luo, M. Manathunga, M. R. Machado, H. M. Nguyen, K. A. O'Hearn, A. V. Onufriev, F. Pan, S. Pantano, R. Qi, A. Rahnamoun, A. Risheh, et al., *J. Chem. Inf. Model.* **2023**, *63*, 6183.
[65] D. Soler-Polo, J. I. Mendieta-Moreno, D. G. Trabada, J. Mendieta, J. Ortega, *J. Chem. Theory Comput.* **2019**, *15*, 6984.
[66] J. I. Mendieta-Moreno, D. G. Trabada, J. Mendieta, J. P. Lewis, P. Gómez-Puertas, J. Ortega, *J. Phys. Chem. Lett.* **2016**, *7*, 4391.
[67] C. Romero-Muñiz, M. Ortega, J. G. Vilhena, I. Díez-Pérez, R. Pérez, J. C. Cuevas, L. A. Zotti, *J. Phys. Chem. C* **2021**, *125*, 1693.
[68] C. Tian, K. Kasavajhala, K. A. A. Belfon, L. Raguette, H. Huang, A. N. Migues, J. Bickel, Y. Wang, J. Pincay, Q. Wu, C. Simmerling, *J. Chem. Theory Comput.* **2020**, *16*, 528.
[69] W. L. Jorgensen, J. Chandrasekhar, J. D. Madura, R. W. Impey, M. L. Klein, *J. Chem. Phys.* **1983**, *79*, 926.
[70] R. T. McGibbon, K. A. Beauchamp, M. P. Harrigan, C. Klein, J. M. Swails, C. X. Hernández, C. R. Schwantes, L. P. Wang, T. J. Lane, V. S. Pande, *Biophys. J.* **2015**, *109*, 1528.